

Interdot Lead Halide Excess Management in PbS Quantum Dot Solar Cells

Miguel Albaladejo-Siguan, David Becker-Koch, Elizabeth C. Baird, Yvonne J. Hofstetter, Ben P. Carwithen, Anton Kirch, Sebastian Reineke, Artem A. Bakulin, Fabian Paulus, and Yana Vaynzof*

Light-harvesting devices made from lead sulfide quantum dot (QD) absorbers are one of the many promising technologies of third-generation photovoltaics. Their simple, solution-based fabrication, together with a highly tunable and broad light absorption makes their application in newly developed solar cells, particularly promising. In order to yield devices with reduced voltage and current losses, PbS QDs need to have strategically passivated surfaces, most commonly achieved through lead iodide and bromide passivation. The interdot spacing is then predominantly filled with residual amorphous lead halide species that remain from the ligand exchange, thus hindering efficient charge transport and reducing device stability. Herein, it is demonstrated that a post-treatment by iodide-based 2-phenylethylammonium salts and intermediate 2D perovskite formation can be used to manage the lead halide excess in the PbS QD active layer. This treatment results in improved device performance and increased shelf-life stability, demonstrating the importance of interdot spacing management in PbS QD photovoltaics.

and near-infrared wavelengths, the latter being particularly important since they represent an essential constituent of the long-tailed solar irradiance spectrum.^[7,8] PbS is especially useful in its quantum dot form, which allows tuning its optoelectronic properties by simply changing the QDs' size, shape, and surface composition.^[9,10] For single junction solar cells, the QD size is selected based on the optimal 1.3 eV bandgap value (E_g), predicted by the thermodynamic theory,^[11] but other applications, such as tandem cells or infrared detectors, benefit from the possibility to tune the PbS QD bandgap from its bulk value of $E_g = 0.37$ eV up to the desired range.^[12–16]

Small nanocrystals of PbS ($E_g = 1.0$ – 1.5 eV) can be conveniently grown in solution, keeping the QDs in an easy-to-handle dispersion throughout the

fabrication process. This ink-like character of the PbS QD solution simplifies the fabrication of devices, opening the route for their large-scale deposition by spraying or inkjet printing.^[14,17,18] Due to their strong and spectrally extended absorption of light, PbS QD solar cells were shown to lead to short-circuit currents (J_{SC}) over 30 mA cm^{-2} and fill factors (FF) as high as 70%. These high photovoltaic performance parameters result in power conversion efficiencies (PCE) of up to 14%,^[19] which can be improved further by minimizing voltage losses in PbS QD devices.


Since Pb chalcogenide quantum dots have an excess of surface Pb atoms,^[20,21] passivation of Pb surface states is crucial for the fabrication of efficient devices. PbS QDs are initially kept stable in suspension by means of long-chained oleate ligands mainly bound to their lead terminated (111) facets.^[22,23] While these oleate molecules ensure colloidal stability, their electronically insulating nature makes it necessary to substitute them with shorter-chained ligands prior to their application in optoelectronic devices.^[24,25] The most common strategy for such a ligand exchange in PbS QD solar cells is based on the use of lead halide salts (PbX_2 , $X = \text{I}$ or Br), which replace the colloid-forming oleate ligands in the liquid phase.^[26] These iodine-rich PbX_2 ligands are of anionic nature and bind preferentially to the lead-rich (111) facets of the PbS QDs, in a similar manner to oleate ligands.^[23] While ligand exchange with PbX_2 significantly improves the efficiency of charge transport in PbS

1. Introduction

Photovoltaic diodes fabricated from lead sulfide (PbS) quantum dots (QDs) have piqued the interest of researchers for over a decade,^[1–3] resulting in a particularly impressive increase in performance in recent years.^[4–6] PbS is well-suited for photovoltaic applications due to its high absorption in the visible

M. Albaladejo-Siguan, D. Becker-Koch, E. C. Baird, Y. J. Hofstetter, A. Kirch, S. Reineke, F. Paulus, Y. Vaynzof
Integrated Center for Applied Physics and Photonic Materials
and Center for Advancing Electronics Dresden (cfaed)
Technische Universität Dresden
01187 Dresden, Germany
E-mail: yana.vaynzof@tu-dresden.de

B. P. Carwithen, A. A. Bakulin
Department of Chemistry and Centre for Processable Electronics
Imperial College London
London W12 0BZ, UK

 The ORCID identification number(s) for the author(s) of this article can be found under <https://doi.org/10.1002/aenm.202202994>.

© 2022 The Authors. Advanced Energy Materials published by Wiley-VCH GmbH. This is an open access article under the terms of the Creative Commons Attribution License, which permits use, distribution and reproduction in any medium, provided the original work is properly cited.

DOI: 10.1002/aenm.202202994

QD thin films, it offers little to no control over the interdot spacing, which, in addition to bound ligands, mostly consists of residual amorphous lead halide species. This is evidenced by the fact that the amount of the Pb halide matrix around PbS QDs has been reported to be as high as 40–50% relative to PbS.^[26,27] Furthermore, the butylamine solvent employed for QD deposition is known to etch Pb halides from the surface of PbS dots, potentially increasing the amount of residual lead halides in between the dots.^[28] Several strategies for managing this interdot spacing have been proposed, both by chemical and physical approaches. Physically, the effect of temperature and annealing of PbS QD films has been studied thoroughly and it has been shown that annealing processes can improve the coupling between dots.^[29] The interdot spacing can be reduced as well by placing the PbS QD films under a solar simulator, but this also triggers degradation of the electronic transport abilities by generating isolated clusters of densely-packed QDs.^[30] Altering the coupling between PbS QDs can be achieved in a chemical manner by modifying the ligands during or after ligand exchange. The chain length of amines used for PbS-PbX₂ ink layer deposition can be optimized to yield a dense QD matrix with increased charge diffusion length.^[26] Introducing very short ligands, such as HI, will reduce the interdot spacing and improve the passivation on the surface, while still keeping electronic confinement effects.^[31]

Degradation effects will also alter the spacing between dots. While oxidation causes dot cores to become more separate,^[32] humid environments tend to fuse dots under heating.^[23] A recent work by Sun et al. provides further insights on this topic, after they soaked the PbS QD layers in a formamidine bromide (FABr) containing solution.^[33] The authors have shown that during this soaking procedure, the lead halide ligands are dissolved from the PbS QDs and react with the FABr to form a 3D perovskite matrix that bridges neighboring dots. Such perovskite interdot bridges increase the diffusion length of charges, as well as the efficiency and stability of solar cells. Similarly, a few studies explore the possibility to control the interdot spacing prior to the deposition of the film. For example, a recent study by Li et al. showed that the incorporation of tetrabutylammonium iodide (TBAI) during the PbS-PbI₂ one-step synthesis can modify the interdot lead halide matrix composition.^[34] The authors claim that the addition of these ammonium salts lowers the excess PbI₂ between neighboring QDs and results in improved performance of the fabricated solar cells. These examples demonstrate the increased interest in controlling the interdot spacing in QD solar cells as a means for further improvements in efficiency and stability.

In this study, we demonstrate a novel post-fabrication treatment approach for interdot space management in PbS QD solar cells. Rather than replacing the lead halide ligands with a perovskite matrix, we demonstrate that it is possible to manage the excess of lead halides by the use of organic iodide salts, typically employed for the formation of 2D perovskites.^[35,36] Phenethylammonium iodide salts have been used as an additive for PbS QD solar cells as reported recently by Yang et al.^[37] The authors claim that the incorporation of small amounts (1 mg mL⁻¹) of these molecules enables the passivation of the PbS quantum dots. We, on the other hand, demonstrate that by treating the PbS QD layer with a solution containing either 2-phenylethylammonium iodide (PEAI), 2-(4-fluorophenyl)ethylamine (F-PEAI), or 2-(4-chlorophenyl)ethylamine (Cl-PEAI) (see Figure S1, Supporting Information, for chemical structures), the interdot excess lead halides can be managed and that no iodide-based 2-phenylethylammonium (X-PEAI) salts remain in the bulk of the PbS film. This occurs via an interaction between these salts and the excess lead halides to form 2D perovskite phases and crystalline PbX₂ domains. Selectively dissolving these 2D perovskites and/or PbX₂ domains results in PbS QD active layers, that when incorporated into solar cells, lead to higher photovoltaic performance and stability. Our results reveal that the choice of organic cation influences the efficacy of its interaction with the excess lead halides, thus, providing important insights for the future application of 2D perovskite cations for interdot space management in PbS QD solar cells.

2. Results

The devices under study were fabricated using a common recipe for PbS QD solar cells that was first reported by Liu et al. in 2016.^[38] In short, PbS QDs were synthesized following a previously reported procedure and exhibited an absorption peak at ≈ 950 nm in solution,^[39,40] which corresponds to a diameter of ≈ 3 nm. Lead halide salts (PbI₂ and PbBr₂) were mixed and used as ligands (in the following referred to as PbX₂) with an iodine-rich molar ratio of 10:4.^[38] Following the ligand exchange, the PbS QD ink was deposited on the solar cell substrates by spin-coating and annealed at 75 °C. Next, a solution of X-PEAI cations in acetonitrile (MeCN) was spin-coated on top of the PbS QD films and the samples were annealed at 75 °C to form the 2D perovskite. Finally, the films were rinsed with neat MeCN to dissolve the formed 2D perovskite. These steps are schematically summarized in **Figure 1**. For comparison, reference samples underwent the identical procedure, yet no X-PEAI salt

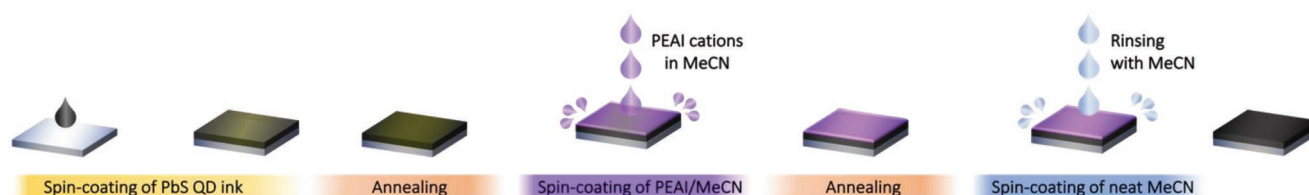


Figure 1. Schematic summary of the fabrication steps of PbS-PbX₂ active layers. The spin coating of the PbS ink is followed by annealing at 75 °C. Then the X-PEAI solution is dispensed on top of the PbS QD layer and spun to dry. After an annealing step at 75 °C to form the 2D perovskite, the films are rinsed with neat acetonitrile and spun until dry.

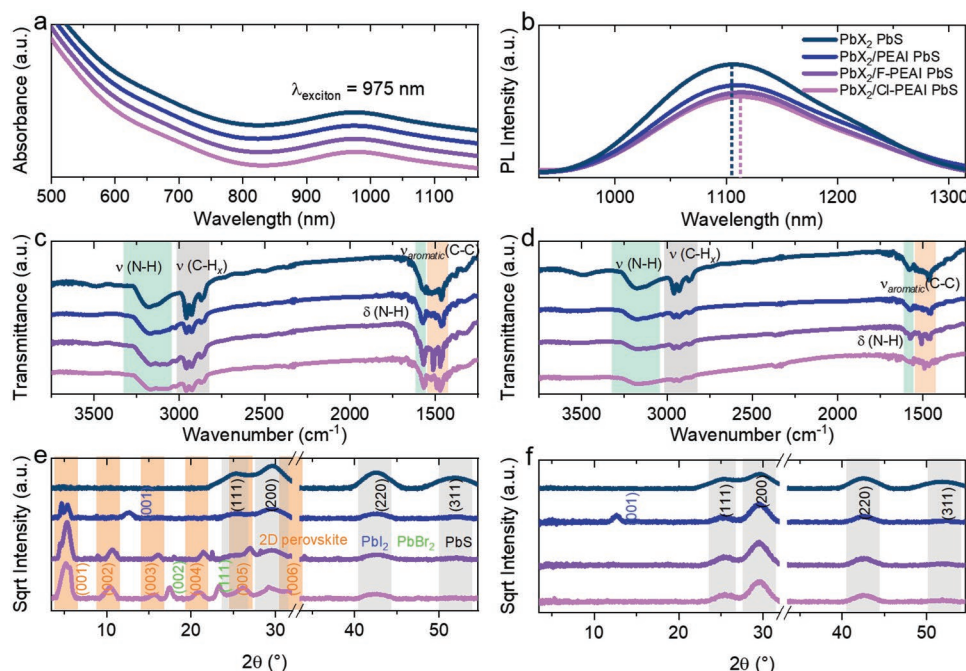


Figure 2. a) UV-vis absorption and b) photoluminescence spectra of PbS QD films upon treatment with X-PEAI salts. FTIR spectra of drop-cast films c) before and d) after the MeCN rinse. XRD measurements on spin-coated X-PEAI salt treated PbS QD films e) before and f) after the MeCN rinse.

was employed in the first MeCN step so that the devices were simply treated with a neat solvent in both steps.

Both the reference and the X-PEAI salt-treated PbS QD films were strongly light-absorbent, dark, and glossy. Ultraviolet-visible (UV-vis) absorption spectra (Figure 2a) showed that the first excitonic peak is located at 975 nm and is unaffected by the X-PEAI salt treatment. There is also no indication of agglomeration or increase of the effective QD size since the peak is not shifted into the infrared (IR). The emission spectra of the various PbS QD films are in the IR (at ≈ 1100 nm), as expected due to the Stokes shift present in PbS QDs.^[41] Figure 2b shows that the X-PEAI treated films result in a slightly red-shifted emission and a small decrease in the photoluminescence (PL) intensity as compared to the reference PbS QD samples. This is particularly evident following the treatment with the two halogenated X-PEAI derivatives. Both of these effects are suggestive of an improved interdot coupling and a faster exciton dissociation,^[42] suggesting that the X-PEAI salt treatment influences the interdot spacing.

To investigate further the influence of treatment with X-PEAI salts on the PbS QD films, we employed Fourier transform infrared (FTIR) spectroscopy and X-ray diffraction (XRD). We note that FTIR measurements on spin-coated PbS layers were too noisy due to their relatively low thickness, so the FTIR measurements shown in Figure 2c,d were measured on drop-cast PbS films. Directly after the treatment with the X-PEAI salts (Figure 2c), two bands originating from the primary amine vibrations can be observed: an N–H stretch centered at 3200 cm^{-1} , and an N–H bend at 1600 cm^{-1} . The first is observed for all of the samples, whereas the second only appears once the PbS has been treated with the X-PEAI salts. The N–H stretch is associated with the presence of the butylamine solvent used in the fabrication of the PbS films since it binds to PbI_2 molecules

through the amine group.^[28] We note that this residual solvent is probably related to the fact that the films were drop-cast, and is likely to be significantly reduced in spin-coated samples. The additional ammonium group from the X-PEAI salts leads to the signal at 1600 cm^{-1} (N–H bend), which is also observed in FTIR measurements of the powder of PEA and its halogenated derivatives (Figure S1, Supporting Information). This molecular vibration is difficult to distinguish from residual butylamine at the surface of the QDs after deposition, which can form a complex with PbI_2 and PbI^+ cations.^[28] Consequently, a small contribution can also be seen for untreated PbX_2 -PbS films. Another feature of the X-PEAI-treated films appears in the region around 1500 cm^{-1} . Here, the aromatic carbons from the phenyl ring create distinct vibrational signatures. These are especially prominent for F-PEAI and Cl-PEAI, where distinct peaks appear (see Figure S1, Supporting Information, for comparison). Upon rinsing the films with MeCN, the features associated with the X-PEAI salts are greatly reduced (Figure 2d), suggesting the vast majority of the X-PEAI salts are removed from the PbS QD samples.

X-ray diffractograms measured on spin-coated PbS QD films treated with X-PEAI salts are shown in Figure 2e. While the reference, untreated films exhibit only the reflections associated with PbS, the X-PEAI-treated films display additional features. All three treated samples show reflections associated with the 2D perovskite $(\text{X-PEA})_2\text{Pb}(\text{Hal})_4$ ($\text{X} = \text{H}, \text{F}, \text{Cl}$; $\text{Hal} = \text{Br}, \text{I}$). All X-PEAI treated samples exhibit more than one distinct peak around 5° . We believe that the presence of iodide and bromide results in the formation of 2D-perovskite with varying mixed halide compositions. The reflections of the 2D-perovskites using F-PEAI and Cl-PEAI are generally shifted to smaller diffraction angles when compared to the PEA-treated samples suggesting an increased lattice spacing. This could either be

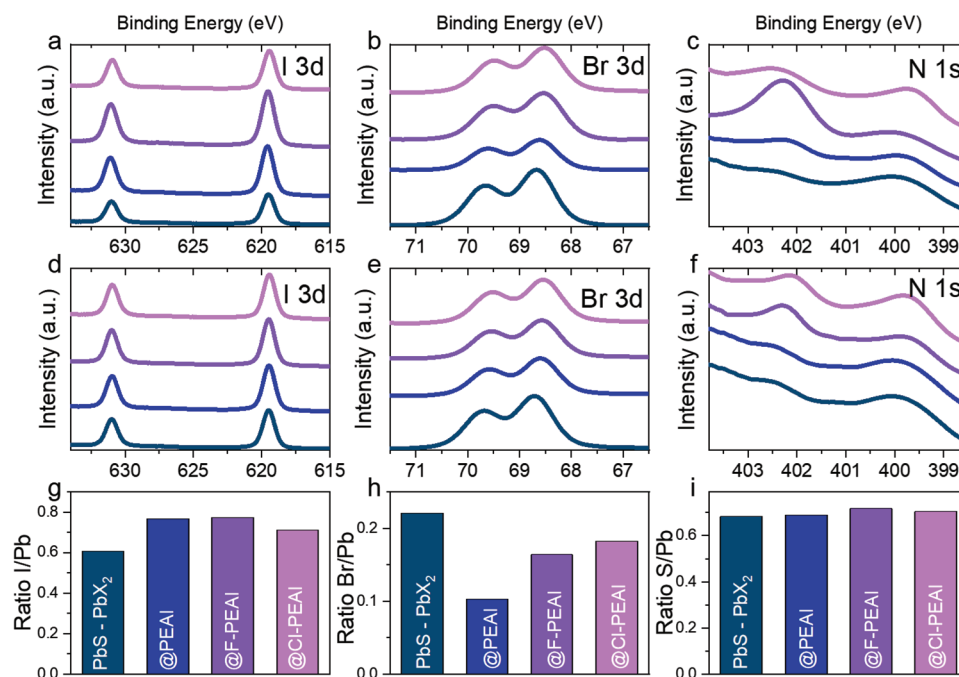


Figure 3. a,d) I3d, b,e) Br3d, and c,f) N1s XPS spectra of PEAI-cations treated samples before/after MeCN rinse. g) I/Pb, h) Br/Pb, and i) S/Pb ratios of PEAI after MeCN rinse.

caused by the slightly larger length of the halogenated PEAI cation or an overall higher iodine content of the perovskites formed with F-PEAI and Cl-PEAI.^[43] In the case of treatment with PEAI, only the main (001) reflex of the 2D perovskites is observed, as well as the (001) reflection of phase-segregated PbI_2 ($2\theta = 12.6^\circ$). The treatment with the halogenated F-PEAI and Cl-PEAI results in more intense reflections from the corresponding 2D perovskites and the entire Bragg series (00l) can be observed. Films treated with Cl-PEAI exhibit phase-separated PbBr_2 domains, evident from the corresponding (002) and (111) reflections in the diffractogram.

Upon rinsing the films with MeCN (Figure 2f), the reflections associated with the 2D perovskite can no longer be observed, suggesting this crystalline material was effectively washed off. Similarly, the reflections associated with PbBr_2 are also removed, while those arising from PbI_2 in the PEAI-treated PbS films remain. The origin of these differences will be discussed in detail at a later point.

Due to the low intensity of the XRD signals (mind the sqrt-scale in Figure 2e,f), we repeated the experiments on thicker, drop-cast PbS QD films (Figure S2, Supporting Information). These experiments confirmed that treatment with PEAI leads to the formation of a 2D perovskite (evident by the presence of the entire (00l) Bragg series), with still lower intensities compared to the corresponding reflections in F-PEAI and Cl-PEAI treated films. Similar to the results on spin-coated films, only PEAI leads to the formation of phase-separated PbI_2 , while phase-separated PbBr_2 appears in the case of the halogenated X-PEAI salts. Upon rinsing these thick, drop-cast films with MeCN, the samples still exhibit small, measurable contributions from 2D perovskite, probably due to the reduced efficacy of MeCN washing away such large amounts of 2D perovskite from the much rougher surface of the drop-casted samples. Similarly to the spin-coated

films, however, the PbI_2 of the PEAI-treated samples remained, while the PbBr_2 can be easily removed by acetonitrile.

To further investigate the changes to the composition of the PbS QD films upon treatment with the X-PEAI salts, the samples were measured via X-ray photoemission spectroscopy (XPS), both before and after rinsing with MeCN. The I 3d, Br 3d, and N 1s spectra are presented in Figure 3, while the Pb 4f, F 1s, and Cl 2p spectra are shown in Figure S3, Supporting Information. Upon treatment with X-PEAI salts, the iodine content in the samples is increased (Figure 3a), which is to be expected since all X-PEAI salts contain iodide. Interestingly, the bromine signal is significantly reduced (Figure 3b), in particular for the PEAI-treated sample. The increased iodine content in the case of PEAI, even after MeCN rinse, is a result of the formation of phase-separated crystalline PbI_2 on the surface, as observed by XRD and confirmed by SEM. On the other hand, treatment with the two halogenated X-PEAI salts shows almost no traces of phase-separated lead halides after the rinsing step. The N1s spectra reveal the presence of two different species: one at 399.5 eV, associated with residual solvent butylamine and one at 402.5 eV, that originates from the nitrogen in the X-PEAI salts. The differences in the intensity of the high binding energy species suggest that different amounts of X-PEAI salts remain in the PbS QD films after treatment. The highest amount is observed for the F-PEAI treated sample, followed by that of Cl-PEAI. This is in agreement with the atomic percentages of fluorine and chlorine (extracted from the F 1s and Cl 2p spectra, Figure S3b,c, Supporting Information), which were found to be 6% and 3%, respectively. Upon rinsing, the excess iodine in the treated samples is greatly reduced (Figure 3d), however, still surpasses that of the reference sample while the bromine content (Figure 3e) remains significantly reduced. The increase in the iodine content and the reduction in the bromine content

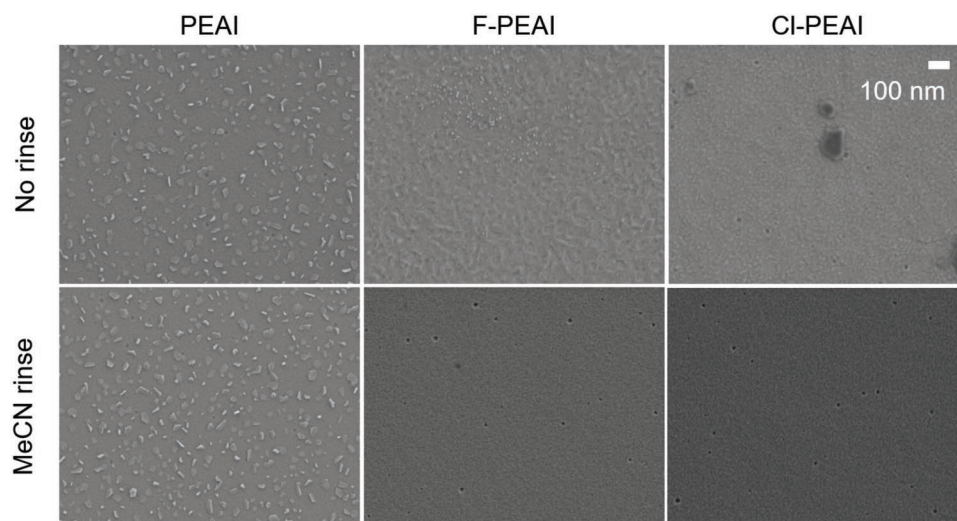


Figure 4. Top view SEM images acquired with Inlens detector of PbS QD films before (top) and after (bottom) treatment with X-PEAI salts and subsequent MeCN rinse. Identical scale bar for all images, given at the top right.

suggest that a halide exchange process occurs during the treatment with the X-PEAI salts. The N1s spectra (Figure 3f) reveal that the intensity of the high binding energy nitrogen species is reduced upon rinsing with MeCN, but is not entirely eliminated from the samples in the washing step. This is supported by the F 1s and Cl 2p spectra, which after rinsing with MeCN, still show clear signals (constituting ≈ 2 atomic %) for each of the halogenated X-PEAI treated samples. Calculating the I/Pb and Br/Pb and S/Pb ratios (Figures 3g, 3h, and 3i, respectively) of the samples after rinsing visualizes the changes in composition that are induced by the X-PEAI treatment. The small increase in the S/Pb ratio (up to 5%) suggests that the treatment led to the removal of some PbX_2 species. S 2p XPS spectra of MeCN-rinsed samples are shown in Figure S4, Supporting Information. In addition, the increase in I/Pb and decrease in Br/Pb ratios led to a significant modification of the I/Br ratio from the initial level of 10:4 introduced during synthesis to 10:1.3 for PEA, 10:2 for F-PEAI, and 10:2.5 for Cl-PEAI. The fact that the changes in the halide content are far larger than those in the lead content confirms that a halide ion exchange process accompanies the removal of the excessive interdot PbX_2 . To investigate if the changes are confined only to the surface of the films or if they impact also its bulk, we performed XPS depth profiling experiments (Figure S5, Supporting Information). The experiments revealed that while the surface is particularly halide rich, the bulk is also impacted by the treatment with X-PEAI. Specifically, upon treatment, the I/Pb ratio is increased, while the Br/Pb ratio is decreased in the bulk of the samples. This furthermore confirms that the removal of excess lead halides from the bulk of the sample is accompanied by halide exchange. Moreover, depth profiling experiments revealed that neither F nor Cl signals are present in the bulk of the sample, suggesting that no X-PEAI remains in the bulk of the film (Figure S6a, Supporting Information). This observation confirms that the treatment with X-PEAI does not lead to the formation of a 2D perovskite shell around the PbS QDs, or a 2D perovskite matrix in between the QDs. The higher presence of halides on the surface of PbS films, even

for reference, favors the formation of 2D perovskite on the surface of the sample. This could be due to the interplay between lead halides and butylamine during the spin-coating and annealing,^[28] forming a lead halide-rich film surface. Diffusion into the densely packed film by the large PEA^+ cations is also unlikely, so the formation of 2D perovskite inside the bulk of the film is not to be expected. This is furthermore confirmed by performing tunneling electron microscopy imaging of Cl-PEAI treated films (Figure S6b, Supporting Information). The diffraction patterns resulting from a Fourier transform of the images reveal exclusively the features associated with PbS, thus, confirming that no 2D perovskite shell remains on the QDs.

The compositional changes observed via XPS suggest that the microstructure of the PbS QD films might also have been altered. To visualize the surface microstructure, all films were further investigated using top-view scanning electron microscopy (SEM), and are shown in Figure 4. Reference PbS QD films exhibit a smooth surface and a compact active layer (Figure S7, Supporting Information). Upon treatment with PEA, small hexagonally shaped crystallites are formed on top of the layer (Figure 4, left) and are not affected by the step of the MeCN rinse. Based on the results of the XRD and the shape of the crystallites, we associate them with crystalline PbI_2 . In the case of the halogenated PEA derivatives, there is a noticeable roughening of the films, which we believe arises from the formation of thin layers and domains of 2D perovskite and in the case of Cl-PEAI, some PbBr_2 domains. These surface features are completely removed after the MeCN rinse and the films appear smooth and structurally intact afterwards, similar to a state prior to X-PEAI application.

To investigate the impact of the X-PEAI treatment on the photovoltaic performance of the QD devices, the PbS QD active layers have been integrated into solar cells with the structure glass/ITO/ZnO/ PbX_2 -PbS/EDT-PbS/Au. Figure 5a–d displays the photovoltaic performance of devices treated with different concentrations of X-PEAI salts normalized to that of reference, untreated devices. Importantly, all of these devices have been fabricated using the same PbS ink and identical

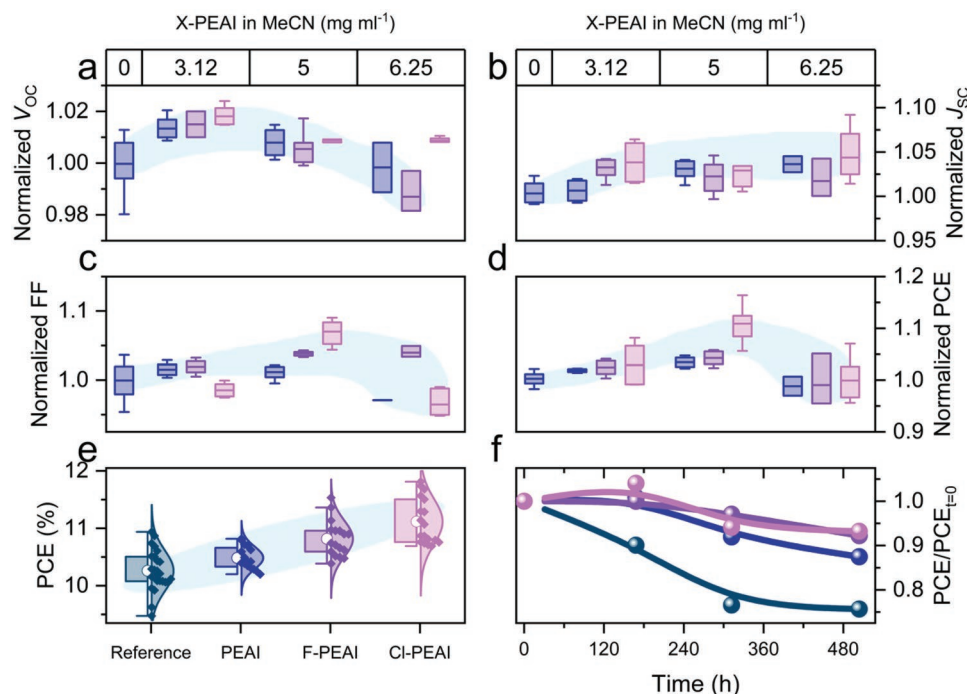


Figure 5. a) Open-circuit voltage, b) short circuit current density, c) fill factor, and d) power conversion efficiency of PbS QD photovoltaic devices as a function of X-PEAI salt concentration in MeCN as top treatment. e) The overall distribution of PCE shows increased performance for all treated devices. f) Lifetime curves of reference and treated devices after dark storage in (30–40% relative humid) air.

processing conditions in one very large batch, and thus, allow for a clear evaluation of the impact of the treatment with X-PEAI of different concentrations. It can be seen that the treatment leads to a small increase in the open-circuit voltage (V_{OC}), especially for the low concentration, but a much more pronounced increase in the J_{SC} and FF. Overall, the optimum PCE is achieved for a concentration of 5 mg mL⁻¹ of X-PEAI and is substantially higher for the Cl-PEAI treated devices, which show an improvement of 10–15%. The increase in J_{SC} is evidenced by a higher external quantum efficiency (EQE) spectra of the treated devices (Figure S8a, Supporting Information), which not only lead to a higher overall response but also show a small shift in the position of the first excitonic peak toward lower energies upon treatment (≈ 10 nm redshift, as observed in PL measurements), which stems from a better interdot coupling similar to the one observed by researchers after FABr treatment.^[27] A redshift of the EQE interference peak at ≈ 750 nm is observed for X-PEAI treated devices, and is likely associated with an increase in the effective refractive index of the film due to the more dense packing of the quantum dots following the X-PEAI treatment. Similar effects have been observed for textured PbS QD devices in the past.^[44,45] Current density-voltage curves of selected pixels under one sun illumination are combined in Figure S8b, Supporting Information. The comparison of the PCE of multiple devices of each kind from different batches is shown in Figure S9, Supporting Information. The highest performance is obtained for the Cl-PEAI treated devices, which reach a maximum PCE of 11.8%. While these data show a broader distribution in photovoltaic performance since they originate from different batches, they clearly demonstrate that the treated devices result in a higher PCE.

To gain insight into the origin of the improved performance, the devices were characterized under different illumination intensities (Figures S10 and S11, Supporting Information). The light intensity-dependent V_{OC} plots show that X-PEAI treated devices show a decreased kT/q slope, which is associated with reduced trap-assisted recombination.^[46] The current versus intensity data suggest only minor differences as compared to the untreated reference solar cells. Furthermore, in order to more directly probe any potential changes to the defect states in the PbS quantum dot solar cells, we applied pump-push-photocurrent (PPPC) spectroscopy which enables us to probe the density and population dynamics of trapped charges in the devices (Figure S12, Supporting Information).^[47] The PPPC experiment is performed on functional solar cells under working conditions and the measured signal is proportional to the concentration of immobile (trapped) carriers at the respective delay times. The decay of the signal is thus assigned to the recombination of the trapped carriers. In agreement with a previous study,^[47] charge trapping in the PbS devices occurred on nanosecond timescales and reached its maximum at ≈ 300 ns. This is followed by ≈ 10 ms recombination. We find that the X-PEAI treatment does not result in the introduction of additional defects, as both the concentration and dynamics of the trapped charges are very similar in both the reference and the treated samples.

The performance of fabricated solar cells was studied over time and characterized as shelf-storage lifetime. The devices were kept unencapsulated in the air (≈ 30 –40% relative humidity, 23 °C) under dark conditions and measured with the solar simulator at diverse time intervals. Figure 5f shows the increased stability of devices treated with X-PEAI salts.

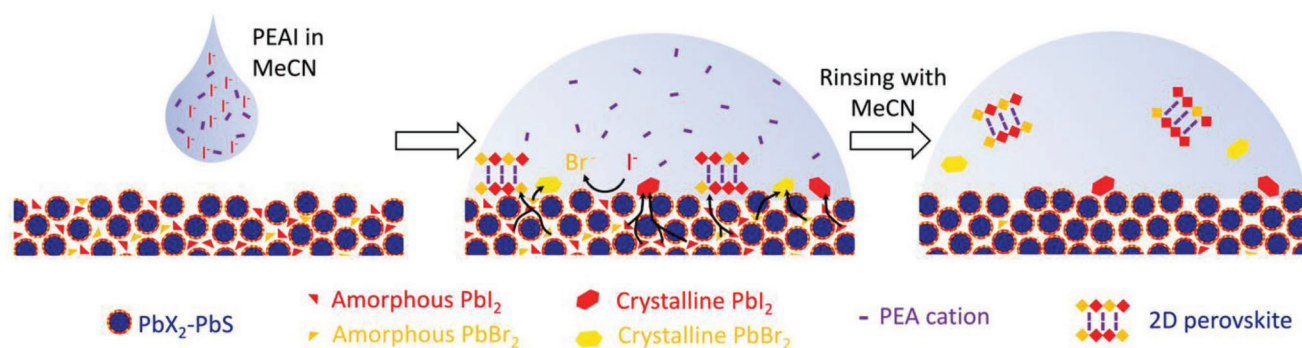


Figure 6. Schematic presentation of the processes that occur during the PEAI cation modification of PbS QDs.

The PCE of the F-PEAI and Cl-PEAI cells maintains 95% of their initial value after 500 h of storage, while the PEAI treated devices drop to 87% of the initial PCE. In comparison, the PCE of the PbX_2 -PbS reference devices dropped to 75% of the initial value within the same time interval. We note that the long-term dark storage stability of our devices is lower than that observed in other reports for devices,^[38] which we attribute to differences in the processing of the devices and the environment (especially relative humidity).^[45] Longer-timescale degradation is dominated mostly by degradation of the hole transport layer (PbS-EDT),^[32,48] and is, therefore, not impacted by the X-PEAI treatment.

The results of the spectroscopic and microscopic characterizations and the improved photovoltaic performance and stability of the solar cells suggest that the treatment with the X-PEAI salts allows for managing the interdot lead halide excess as well as effectively modifying the surface composition of the solar cells' active layer. To confirm the improved interdot coupling in treated devices, the hole mobility was measured in unipolar device structures. For this purpose, hole-only devices consisting of ITO/PbS-EDT/PbS- PbX_2 (150 nm)/PbS-EDT/Au were fabricated for both reference and X-PEAI-treated devices. The mobilities extracted by the space charge limited current method ($J \sim V^2$), shown in Figure S13, Supporting Information, are a factor of two higher for F-PEAI and Cl-PEAI treated devices, corroborating that this treatment leads to improved interdot coupling. To further confirm the changes in the interdot spacing and the resulting improved interdot coupling, we performed TEM measurements in which the ligand exchange and subsequent treatment with X-PEAI were performed directly on the TEM grid, following the procedure reported by Teh et al. to quantify the interdot spacing after a thiol ligand exchange.^[49] In the exemplary case of F-PEAI, the interdot spacing is reduced from 1.2 to 0.8 nm (Figure S14, Supporting Information). We highlight that this dot-to-dot distance is larger than the one in the solid state PbS- PbX_2 films as measured by grazing-incidence small-angle X-ray scattering (GISAXS), which is around 1–2 Å,^[27] and stems from the deposition technique on TEM grids from heavily diluted inks. This decrease leads to improved interdot coupling, which is evidenced by a reduction in the PL lifetime of treated samples probed by time-correlated single photon counting (TCSPC) experiments (Figure S15, Supporting Information). The TCSPC measurements show that the lifetime of PbX_2 -PbS reference samples is reduced from 2.3 to

1.8 ns upon treatment with F-PEAI. This decrease is related to the improved exciton dissociation in quantum dot films with reduced interdot spacing.

Since treatment of the quantum dot active layer with pure MeCN in the reference devices does not lead to such modifications, the presence of the PEAI components in the MeCN must facilitate the changes in layer and surface composition (Figure 6). Upon the addition of the X-PEAI salts in the first MeCN step, followed by a gentle drying at 75 °C, 2D-perovskite domains are formed on top of the active layer. We believe that the presence of X-PEA^+ and I^- ions increases the chemical mobility of lead halides toward the surface of the porous quantum dot film, leading to the effective extraction of lead halides from the active layer itself. It is fair to assume that lead halide aggregation, crystallization and perovskite formation, and the interaction with X-PEAI act as the thermodynamic driving force for this process. We emphasize, that the concentration, and therefore, the overall amount of the X-PEAI salt is crucial and needs to be finely adjusted (Figure 5a–d). Effective removal of the lead halide excess and best PV performance was found for a concentration of 5 mg mL⁻¹ in the case of Cl-PEAI. Higher concentrations lead to a degradation of the device efficiency and could indicate that not only excessive lead halides are being removed from the film but also the PbX_2 ligand shell around the quantum dots might be affected or even etched when higher amounts of X-PEAI salts are being used.

Since lead iodide and lead bromide are present in the active layer, we expect that the overall amount and ratio of phase-separated lead iodide, lead bromide, and perovskites domains, as well as the halide composition of the 2D-perovskite itself, strongly depend on the interaction of the interdot lead halides with the X-PEAI salt. In the case of PEAI, we observed phase-separated PbI_2 domains, which suggests a higher bromide content in the 2D-perovskite domains. While for Cl-PEAI and F-PEAI, the opposite effect occurs, and phase-separated lead bromide is formed. When washing the films after X-PEAI treatment with MeCN, only the lead iodide domains remain while the lead bromide ones are washed off. This can easily be explained by the approximately ten times higher solubility of pure lead bromide in MeCN compared to lead iodide (see Figure S16, Supporting Information). The formed 2D perovskites exhibit a sufficiently large solubility in the applied volume of MeCN and are removed from the film's surface in all three cases and only very minor traces ($\approx 2\%$) of X-PEAI remain.

To further quantify the excess Pb halide removal from the film, we calculated the weight loss after drop casting treatment and a subsequent MeCN rinse (Figure S17, Supporting Information).

Considering the suggested mechanism for excess lead halide removal above, it is important to notice that all steps involve the interplay and competition of two different anions. While the employed X-PEAI salts are all iodide based, the excess of lead halide PbX_2 in the quantum dot film contains bromide and iodide. That in turn means that exchange processes between iodide and bromide will occur and might even reach an equilibrium state within the application time of the MeCN solution. Generally, the use of iodide-based salts in the solvent will cause in all cases a shift of the I/Br ratio to higher iodine contents. However, the exact ratio will depend on the differences in solubility, crystallization dynamics, and formation enthalpy between the corresponding bromide and iodide species. For example, the overall ratio of solvated bromide and iodide in the first MeCN step that will be removed by spinning off the MeCN solution after a contact time of 20 s will most likely depend on the differences in solubility of the corresponding X-PEAI and X-PEABr salts. Our experiments indicate that PEAI alters the initial I/Br ratio more severely, while F-PEAI causes the smallest change in the halide ratio. The underlying reason for a higher device performance with F-PEAI and Cl-PEAI in our study is related to the fact that these molecules have a higher dipole moment than pure PEAI,^[37] thus, triggering a different effect in excess removal and later solubility of products on the surface.

3. Conclusion

This work presents a facile approach to increase the efficiency and shelf life of PbS QD solar cells by 2D perovskite cation-mediated removal of excess interdot lead halides. We demonstrate that upon the addition of small concentrations of PEAI, Cl-PEAI, or F-PEAI salts, excess PbI_2 and PbBr_2 between the quantum dots can be extracted and transformed into 2D perovskites or crystalline PbX_2 on the surface of the QD films. These can be later washed off, “rinsed” or “rinsed off”, leading to a film with increased interdot coupling, improved photovoltaic performance, and enhanced stability. Our work opens a new route for the effective management of excess lead halides in lead chalcogenide solar cells and other optoelectronic devices.

4. Experimental Section

Materials and Purity: Lead (II) oxide (Alfa Aesar Puratronic, 99.999%), oleic acid (Alfa Aesar, 90% technical grade), octadecene (Alfa Aesar, 90% technical grade), and hexamethyldisilathiane (TMS_2S Sigma-Aldrich, synthesis grade) were employed as received for PbS QD synthesis. Lead (II) iodide and lead (II) bromide (TCI, 99.99% trace metal basis), ammonium acetate (Fisher Chemical, >97%), and *N,N*-dimethylformamide (DMF) (Acros Organics, 99.8% ExtraDry) were used in the ligand exchange. PEAI, F-PEAI, and Cl-PEAI were purchased from Greatcell Solar Materials and have a purity of >99%. They should be stored in a nitrogen glovebox since they will absorb water. All organic solvents used in this study were from Acros Organics.

PbS QD Synthesis: For a usual batch of QDs, the hot-injection synthesis recipe was adapted from previous works.^[39] In order to get PbS QDs with a bandgap of 1.3 eV, PbO (451 mg), OA (1.5 mL), and

ODE (18 mL) were degassed in a 10^{-3} mbar vacuum under 100 °C using Schlenk techniques. After 2 h, TMS_2S (180 μL) was swiftly injected into the clear solution under nitrogen. Instantly the nucleation started, and the color changed to dark brown. The reacted product was collected and purified using acetone (1:1 by volume) and methanol/butanol (1:8 by volume), always collecting the QDs by 10-min centrifugation at 5000 rpm after adding the antisolvents. For smaller dots in the PbS-EDT layer, the recipe was the same except for the injection temperature, which was reduced to 90 °C to get smaller dots.

PbS-PbX₂ Ligand Exchange: For a typical ligand exchange, a mixed lead halide precursor was prepared in DMF. PbI_2 (0.1 M), PbBr_2 (0.04 M), and ammonium acetate (0.04 M) were dissolved in DMF (20 mL). This yellow precursor was added to PbS (20 mL) QDs in octane (10 mg mL^{-1}). After vigorous mixing, the black DMF phase was collected and washed three times with pure *n*-octane. The remaining liquid was then placed in a centrifuge tube and after adding toluene (1:0.75 by volume), it was centrifuged for 5 min at 5000 rpm. The supernatant was discarded, and the remaining pellet was dried under vacuum for an hour. The pellet (normally around 150 mg) can be stored in an inert atmosphere for at least a week before making the solar cells.

Device Fabrication: Pre-patterned glass/indium tin oxide (ITO) substrates ($12 \times 12 \times 1$ mm) were cleaned using acetone and isopropanol in a sonication bath. The surface was activated with oxygen plasma for 10 min. A thin ZnO sol-gel layer was spun at 3000 rpm on the substrate and annealed at 300 °C, following published methods.^[50] The stored PbS-PbX₂ pellet was dissolved in *n*-butylamine with a concentration of 400 mg mL^{-1} , depending on the desired thickness. This dense ink was spin-coated on the substrates for 20 s at 2500 rpm and dried on a hotplate for 10 min at 75 °C. This step was performed in a nitrogen glovebox to ensure reproducible results. For solar cells with additional treatment, a solution of either PEAI, F-PEAI, or Cl-PEAI (5 mg mL^{-1}) was prepared with dry acetonitrile (MeCN). This solution was dropped on top of the active layer and spun after 20 s at 3000 rpm to remove excess solvent. The substrates were placed again on a plate at 75 °C to form the 2D perovskite (10 min) and then they were rinsed with neat MeCN on the spin coater. Two layers of PbS-EDT were spin-coated in the air using already published methods.^[39] It is important to note that PbS dots were used with a first excitonic peak around 850 nm for this layer, to provide a better blocking of electrons in the solar cells. 80 nm thick Au pixels were thermally evaporated (10^{-6} mbar) on top to give 4.5 mm^2 solar cells. There was a total of eight solar cells per substrate.

Absorbance and Luminescence: The absorbance and photoluminescence (PL) of the PbS QDs were measured on films made on glass by spin-coating. The absorbance spectra were measured with a Shimadzu SolidSpec 3700. The PL signal was acquired using a green LED (Thorlabs, M505L3) as the excitation source and an NIR InGaAs spectrometer (Instrument Systems, CAS 140CT IR1) as the detection unit. To assess the exciton lifetime of the quantum dots, QD films with a photoluminescence peak centered around 950 nm were investigated. Corresponding TCSPC measurements were conducted in the air utilizing a pulsed 405 nm laser (LDH-IB diode laser and Taiko PDL M1 controller, both PicoQuant GmbH) as the excitation source. To ensure only the emitted photons from the QD layer were counted, an 850 nm longpass filter (Thorlabs) was used. The measurements utilized a fiber-coupled PDM SPAD (Micro Photon Devices) and the PicoHarp 300 electronics (PicoQuant GmbH) with an integration time of 96 min. The PL decay was fitted using a convolution of an exponential and Gaussian function.

Infrared Spectroscopy: FTIR spectra were taken with a Shimadzu IR Spirit. The samples were drop-casted on single side polished silicon substrates and measured in transmission mode.

X-Ray Photoemission Spectroscopy: XPS measurements were carried out in an ultrahigh vacuum chamber (ESCALAB 250Xi by Thermo Scientific, base pressure: 2×10^{-10} mbar) using an XR6 monochromated Al K α source ($h\nu = 1486.6$ eV) and a pass energy of 20 eV. XPS depth profiling was performed using an argon gas cluster ion beam with large argon clusters (Ar_{2000}) and an energy of 4 keV generated by a MACCIS dual mode ion source. XPS spectra were evaluated using the Advantage software by Thermo Scientific. First, a suitable background was added

to each spectrum, then the peaks were fitted using Gaussian–Lorentzian functions. Fits of doublet peaks were restrained regarding spin-orbit splitting, peak area ratio, and FWHM. Finally, the software was used to calculate the atomic percentage contribution of each element using the resulting peak areas and their respective atomic sensitivity factors. The fitted spectra shown in Figure 3 are shown in Figures S18 and S19, Supporting Information.

X-Ray Diffraction: PbS films drop-casted or spun on silicon wafers were analyzed using a Bruker D8 Discover diffractometer equipped with a 1.6 kW Cu X-ray filament ($\lambda = 1.5 \text{ \AA}$) and a 0.6 mm slit. The scans were performed using a 1D detector in the $\theta/2\theta$ mode.

Scanning Electron Microscopy: Images were acquired on a Zeiss Gemini 600 SEM in high-resolution mode. The acceleration voltage was set to 1.5 kV to avoid strong degradation of the sample due to charging.

Transmission Electron Microscopy: The TEM images were acquired on a Jeol JEM F200 operated at 200 kV in transmission mode and images were taken on a Gatan 4k video camera. Samples were drop-casted from a dilute PbS QD ink directly on TEM carbon/copper grids and dried in a glass oven before mounting into the TEM holder. The ligand exchange was also performed directly on the TEM grid.

Solar Cell Characterization: Solar cells were measured under an Abet A+++ solar simulator, with a simulated AM1.5 spectrum that was calibrated using a Newport reference silicon solar cell (100 mW cm^{-2}). The forward-backward voltage sweep (-0.1 to 0.7 V in 0.025 V steps) was done with a Keithley 2450 source measure unit (SMU). The intensity-dependent JV curves were acquired by placing diverse optical filters (Thorlabs absorptive ND filter kit) with known optical density on top of the measured solar cells. EQE spectra were measured with a self-built setup. A halogen lamp passed through a monochromator was used to generate a current in the solar cells, which was measured with a Keithley SMU. This current was corrected for the irradiance of the lamp using a calibrated silicon and InGaAs diode and the efficiency to generate an electron for every irradiated photon was calculated.

Pump-Push-Photocurrent Measurements: PPPC measurements were performed using the output of a Pico (Innolas, $\lambda = 1064 \text{ nm}$, $\tau \approx 2 \text{ ns}$, pulse energy $\approx 0.25 \text{ nJ}$) laser as the “pump” and an optical parametric amplifier (TOPAS-Prime, Coherent, $\lambda_c = 2073 \text{ nm}$, $\tau \sim 100 \text{ fs}$, pulse energy $\approx 2 \text{ \mu J}$), seeded by a Ti:sapphire regenerative amplifier (Astrella, Coherent), as the “push”. Pump and push beams were focused onto a $\approx 400 \text{ \mu m}$ -diameter spot at the samples. The pump reference current (I) was read out by a lock-in amplifier (MFLI, Zurich Instruments) at 4 kHz , and the push-induced current (ΔI) was modulated at 717 Hz by an optical chopper. The pump-push delay time was controlled by triggering the pump via a delay generator (SRS DG645, Lambda). Due to the delay generator jitter, the time resolution of the experiment was on the order of 20 ns . After the measurements, data were corrected for bimolecular recombination effects, which were estimated by using the dynamics at negative delay times. Data were normalized by the reference current I and the $\Delta I/I$ values were used for the interpretation of the results.^[47]

Supporting Information

Supporting Information is available from the Wiley Online Library or from the author.

Acknowledgements

The authors acknowledge financial support from the European Research Council (ERC) under the European Union's Horizon 2020 research and innovation program (ERC Grant Agreements No. 714067, ENERGYMAPS). The authors thank the Deutsche Forschungsgemeinschaft (DFG) for funding the project “PROCES” (VA 991/2-1). The authors would also like to acknowledge the Dresden Center for Nanoanalysis for providing the opportunity to perform electron microscopy experiments. A.K. received

funding from the Cusanuswerk Foundation and acknowledges funding from the DFG project HEFOS (Grant No. FI 2449/1-1).

Open access funding enabled and organized by Projekt DEAL.

Conflict of Interest

The authors declare no conflict of interest.

Data Availability Statement

The data that support the findings of this study are available from the corresponding author upon reasonable request.

Keywords

2D perovskites, passivation, quantum dots, solar cells

Received: September 1, 2022
Published online: October 3, 2022

- [1] K. W. Johnston, A. G. Pattantyus-Abraham, J. P. Clifford, S. H. Myrskog, D. D. MacNeil, L. Levina, E. H. Sargent, *Appl. Phys. Lett.* **2008**, 92, 5.
- [2] D. A. R. Barkhouse, A. G. Pattantyus-Abraham, L. Levina, E. H. Sargent, *ACS Nano* **2008**, 2, 2356.
- [3] J. Gao, J. M. Luther, O. E. Semonin, R. J. Ellingson, A. J. Nozik, M. C. Beard, *Nano Lett.* **2011**, 11, 1002.
- [4] K. Bertens, J. Z. Fan, M. Biondi, A. S. Rasouli, S. Lee, P. Li, B. Sun, S. Hoogland, F. P. G. De Arquer, Z. H. Lu, E. H. Sargent, *ACS Mater. Lett.* **2020**, 2, 1583.
- [5] C. Ding, F. Liu, Y. Zhang, S. Hayase, T. Masuda, R. Wang, Y. Zhou, Y. Yao, Z. Zou, Q. Shen, *ACS Energy Lett.* **2020**, 5, 3224.
- [6] M. Al Mubarak, F. Tri, A. Wibowo, H. Aqoma, N. V. Krishna, W. Lee, D. Y. Ryu, S. Cho, I. H. Jung, S. Jang, *ACS Energy Lett.* **2020**, 5, 3452.
- [7] J. Z. Fan, M. Vafaie, K. Bertens, M. Sytnyk, J. M. Pina, L. K. Sagar, O. Ouellette, A. H. Proppe, A. S. Rasouli, Y. Gao, S. W. Baek, B. Chen, F. Laquai, S. Hoogland, F. P. G. De Arquer, W. Heiss, E. H. Sargent, *Nano Lett.* **2020**, 20, 5284.
- [8] A. Karani, L. Yang, S. Bai, M. H. Futscher, H. J. Snaith, B. Ehrler, N. C. Greenham, D. Di, *ACS Energy Lett.* **2018**, 3, 869.
- [9] H. Choi, J. H. Ko, Y. H. Kim, S. Jeong, *J. Am. Chem. Soc.* **2013**, 135, 5278.
- [10] P. R. Brown, D. Kim, R. R. Lunt, N. Zhao, M. G. Bawendi, J. C. Grossman, V. Bulović, *ACS Nano* **2014**, 8, 5863.
- [11] W. Shockley, H. J. Queisser, *J. Appl. Phys.* **1961**, 32, 510.
- [12] M. M. Tavakoli, H. T. Dastjerdi, P. Yadav, D. Prochowicz, H. Si, R. Tavakoli, *Adv. Funct. Mater.* **2021**, 31, 2010623.
- [13] Y. Zhang, M. Gu, N. Li, Y. Xu, X. Ling, Y. Wang, S. Zhou, F. Li, F. Yang, K. Ji, J. Yuan, W. Ma, *J. Mater. Chem. A* **2018**, 6, 24693.
- [14] A. Yousefamin, N. A. Killilea, M. Sytnyk, P. Maisch, K. C. Tam, H. J. Egelhaaf, S. Langner, T. Stubhan, C. J. Brabec, T. Rejek, M. Halik, K. Poulsen, J. Niehaus, A. Köck, W. Heiss, *ACS Nano* **2019**, 13, 2389.
- [15] A. De Iacovo, C. Venettacci, L. Colace, L. Scopa, S. Foglia, *Sci. Rep.* **2016**, 6, 37913.
- [16] H. Jeong, J. H. Song, S. Jeong, W. S. Chang, *Sci. Rep.* **2020**, 10, 12475.

- [17] R. Sliz, M. Lejay, J. Z. Fan, M. J. Choi, S. Kinge, S. Hoogland, T. Fabritius, F. P. G. De Arquer, E. H. Sargent, *ACS Nano* **2019**, *13*, 11988.
- [18] M. J. Choi, Y. J. Kim, H. Lim, E. Alarousu, A. Adhikari, B. S. Shaheen, Y. H. Kim, O. F. Mohammed, E. H. Sargent, J. Y. Kim, Y. S. Jung, *Adv. Mater.* **2019**, *31*, 1970225.
- [19] H. Il Kim, S. W. Baek, H. J. Cheon, S. U. Ryu, S. Lee, M. J. Choi, K. Choi, M. Biondi, S. Hoogland, F. P. G. de Arquer, S. K. Kwon, Y. H. Kim, T. Park, E. H. Sargent, *Adv. Mater.* **2020**, *32*, 2004985.
- [20] D. M. Balazs, K. I. Bijlsma, H. H. Fang, D. N. Dirin, M. Döbeli, M. V. Kovalenko, M. A. Loi, *Sci. Adv.* **2017**, *3*, eaao1558.
- [21] I. Moreels, Y. Justo, B. De Geyter, K. Hastraete, J. C. Martins, Z. Hens, *ACS Nano* **2011**, *5*, 2004.
- [22] Y. Wang, K. Lu, L. Han, Z. Liu, G. Shi, H. Fang, S. Chen, T. Wu, F. Yang, M. Gu, S. Zhou, X. Ling, X. Tang, J. Zheng, M. A. Loi, W. Ma, *Adv. Mater.* **2018**, *30*, 1704871.
- [23] G. Shi, H. Wang, Y. Zhang, C. Cheng, T. Zhai, B. Chen, X. Liu, R. Jono, X. Mao, Y. Liu, X. Zhang, X. Ling, Y. Zhang, X. Meng, Y. Chen, S. Duhm, L. Zhang, T. Li, L. Wang, S. Xiong, T. Sagawa, T. Kubo, H. Segawa, Q. Shen, Z. Liu, W. Ma, *Nat. Commun.* **2021**, *12*, 4381.
- [24] C. R. Kagan, E. Lifshitz, E. H. Sargent, D. V. Talapin, *Science* **2016**, *353*, aac5523.
- [25] C. R. Kagan, C. B. Murray, *Nat. Nanotechnol.* **2015**, *10*, 1013.
- [26] J. Xu, O. Voznyy, M. M. Liu, A. R. Kirmani, G. Walters, R. Munir, M. Abdelsamie, A. H. Proppe, A. Sarkar, F. P. G. De Arquer, M. Wei, B. Sun, M. M. Liu, O. Ouellette, R. Quintero-Bermudez, J. Li, J. Fan, L. Quan, P. Todorovic, H. Tan, S. Hoogland, S. O. Kelley, M. Stefik, A. Amassian, E. H. Sargent, *Nat. Nanotechnol.* **2018**, *13*, 456.
- [27] B. Sun, A. Johnston, C. Xu, M. Wei, Z. Huang, Z. Jiang, H. Zhou, Y. Gao, Y. Dong, O. Ouellette, X. Zheng, J. Liu, M. J. Choi, Y. Gao, S. W. Baek, F. Laquai, O. M. Bakr, D. Ban, O. Voznyy, F. P. G. de Arquer, E. H. Sargent, *Joule* **2020**, *4*, 1542.
- [28] J. Yang, M. Kim, S. Lee, J. W. Yoon, S. Shome, K. Bertens, H. Song, S. G. Lim, J. T. Oh, S. Y. Bae, B. R. Lee, W. Yi, E. H. Sargent, H. Choi, *ACS Appl. Mater. Interfaces* **2021**, *13*, 36992.
- [29] W. Lü, F. Yamada, I. Kamiya, J. Vac. Sci. Technol., B: Nanotechnol. Microelectron.: Mater., Process., Meas., Phenom. **2010**, *28*, C5E8.
- [30] W. Chen, R. Guo, H. Tang, K. S. Wienhold, N. Li, Z. Jiang, J. Tang, X. Jiang, L. P. Kreuzer, H. Liu, M. Schwartzkopf, X. W. Sun, S. V. Roth, K. Wang, B. Xu, P. Müller-Buschbaum, *Energy Environ. Sci.* **2021**, *14*, 3420.
- [31] J. W. Jo, J. Choi, F. P. G. De Arquer, A. Seifitokaldani, B. Sun, Y. Kim, H. Ahn, J. Fan, R. Quintero-Bermudez, J. Kim, M. J. Choi, S. W. Baek, A. H. Proppe, G. Walters, D. H. Nam, S. Kelley, S. Hoogland, O. Voznyy, E. H. Sargent, *Nano Lett.* **2018**, *18*, 4417.
- [32] D. Becker-Koch, M. Albaladejo-Siguan, V. Lami, F. Paulus, H. Xiang, Z. Chen, Y. Vaynzof, *Sustainable Energy Fuels* **2019**, *4*, 108.
- [33] B. Sun, A. Johnston, C. Xu, M. Wei, Z. Huang, Z. Jiang, H. Zhou, Y. Gao, Y. Dong, O. Ouellette, X. Zheng, J. Liu, M. J. Choi, Y. Gao, S. W. Baek, F. Laquai, O. M. Bakr, D. Ban, O. Voznyy, F. P. G. de Arquer, E. H. Sargent, *Joule* **2020**, *4*, 1542.
- [34] F. Li, Y. Liu, G. Shi, W. Chen, R. Guo, D. Liu, Y. Zhang, Y. Wang, X. Meng, X. Zhang, Y. Lv, W. Deng, Q. Zhang, Y. Shi, Y. Chen, K. Wang, Q. Shen, Z. Liu, P. Müller-Buschbaum, W. Ma, *Adv. Funct. Mater.* **2021**, *31*, 2104457.
- [35] G. Grancini, C. Roldán-Carmona, I. Zimmermann, E. Mosconi, X. Lee, D. Martineau, S. Narbey, F. Oswald, F. De Angelis, M. Graetzel, M. K. Nazeeruddin, *Nat. Commun.* **2017**, *8*, 15684.
- [36] T. Zhu, D. Zheng, J. Liu, L. Coolen, T. Pauporte, *ACS Appl. Mater. Interfaces* **2020**, *12*, 37197.
- [37] X. Yang, J. Yang, M. I. Ullah, Y. Xia, G. Liang, S. Wang, J. Zhang, H. Y. Hsu, H. Song, J. Tang, *ACS Appl. Mater. Interfaces* **2020**, *12*, 42217.
- [38] M. Liu, O. Voznyy, R. Sabatini, F. P. G. De Arquer, R. Munir, A. H. Balawi, X. Lan, F. Fan, G. Walters, A. R. Kirmani, S. Hoogland, F. Laquai, A. Amassian, E. H. Sargent, *Nat. Mater.* **2017**, *16*, 258.
- [39] M. Albaladejo-Siguan, D. Becker-Koch, A. D. Taylor, Q. Sun, V. Lami, P. G. Oppenheimer, F. Paulus, Y. Vaynzof, *ACS Nano* **2020**, *14*, 384.
- [40] M. A. Hines, G. D. Scholes, *Adv. Mater.* **2003**, *15*, 1844.
- [41] Y. Liu, D. Kim, O. P. Morris, D. Zhitomirsky, J. C. Grossman, *ACS Nano* **2018**, *12*, 2838.
- [42] L. Sun, J. J. Choi, D. Stachnik, A. C. Bartnik, B. R. Hyun, G. G. Malliaras, T. Hanrath, F. W. Wise, *Nat. Nanotechnol.* **2012**, *7*, 369.
- [43] Q. Zhou, L. Liang, J. Hu, B. Cao, L. Yang, T. Wu, X. Li, B. Zhang, P. Gao, *Adv. Energy Mater.* **2019**, *9*, 1802595.
- [44] T. Kim, X. Jin, J. H. Song, S. Jeong, T. Park, *ACS Energy Lett.* **2020**, *5*, 248.
- [45] G. F. Burkhard, E. T. Hoke, M. D. McGehee, *Adv. Mater.* **2010**, *22*, 3293.
- [46] N. Thongprong, T. Supasai, Y. Li, I. M. Tang, N. Rujsamphan, *Energy Technol.* **2020**, *8*, 1901196.
- [47] A. A. Bakulin, S. Neutzner, H. J. Bakker, L. Ottaviani, D. Barakel, Z. Chen, *ACS Nano* **2013**, *7*, 8771.
- [48] D. Becker-Koch, M. Albaladejo-Siguan, Y. J. Hofstetter, O. Solomeshch, D. Pohl, B. Rellinghaus, N. Tessler, Y. Vaynzof, *ACS Appl. Mater. Interfaces* **2021**, *13*, 18750.
- [49] Z. L. Teh, L. Hu, Z. Zhang, A. R. Gentle, Z. Chen, Y. Gao, L. Yuan, Y. Hu, T. Wu, R. J. Patterson, S. Huang, *ACS Appl. Mater. Interfaces* **2020**, *12*, 22751.
- [50] Y. Sevinchan, P. E. Hopkinson, A. A. Bakulin, J. Herz, M. Motzkus, Y. Vaynzof, *Adv. Mater. Interfaces* **2016**, *3*, 1500616.